Supplement of Atmos. Meas. Tech., 15, 11–19, 2022
https://doi.org/10.5194/amt-15-11-2022-supplement
© Author(s) 2022. CC BY 4.0 License.

Atmospheric Measurement Techniques
Open Access
EGU

Supplement of

A study on the fragmentation of sulfuric acid and dimethylamine clusters inside an atmospheric pressure interface time-of-flight mass spectrometer

Dina Alfaouri et al.

Correspondence to: Hanna Vehkamäki (hanna.vehkamaki@helsinki.fi)

The copyright of individual parts of the supplement might differ from the article licence.

Supporting Information

S1. Experimental Set-up

The experiments in this study were conducted using a set-up consisting of a combination of ElectroSpray Ionization, planar Differential Mobility Analyser and Atmospheric Pressure interface Time Of Flight mass spectrometer (ESI–DMA–APi-TOF MS). The main text includes a schematic representation of the set-up (Fig. 1). The APi-TOF was operated in negative mode, and all data analysis were performed using tofTools; a set of Matlab-based programs developed at the University of Helsinki. We were investigating clusters of sulfuric acid and dimethylamine. A 100 mM/100 mM dimethylamine/sulfuric acid solution in methanol and water with a ratio of 4:1 v:v was used to produce negatively charged clusters. The solution was charged by applying a negative voltage by the ESI, and then electrosprayed via a pressure gradient applied to the solution to allow it to pass through a silica capillary (30 μm tip, 75 μm i.d., 360 μm o.d., non-coated, SilicaTip TM, PicoTip TM EMITTER, NewObjective). Separation of the charged clusters was achieved using a planar DMA P5 (SEADM, Valladolid, Spain), with the sheath flow blower operating at 18000 rpm (for further information on this DMA see (Amo-González and Pérez, 2018). The carrier gas used in the sheath flow was nitrogen (N_2) gas. The outlet of the DMA was connected to an electrometer (SEADM, model LYNX-E11) with an inlet flow rate of 1 L/min and to the APi-TOF (Tofwerk AG, Thun, Switzerland) with an inlet flow rate of 0.8 L/min. The APi part consists of three chambers, which are connected to a scroll pump and a turbo pump which allows for a successive pressure drop across the chambers reaching a pressure of about 10-6 mbar towards the third (final) chamber. The first two chambers hold two quadrupoles (Q1 and Q2), whose main purpose is to guide the charged clusters through. The third chamber uses multiple lenses to focus the beam of ions/charged clusters. A detailed description of the instrument can be found in (Junninen et al., 2010).

S2. Chemicals

The following chemicals were used without further purification; sulfuric acid (H2SO4) (95-97%), and dimethyleamine ((CH3)2NH) (40 wt. % in H2O) which were obtained from Sigma Aldrich. Solutions were prepared using methanol HPLC fluorescence grade (purchased from Fisher Chemical) and deionized ultra-pure aerated Milli-Q water from Millipore.

S3. TOF power supply voltage settings

TOF Power Supply (TPS) voltage settings of the APi-TOF are usually changed to optimize the results. The optimization process depends on the specifics of the study. Overall, two radio frequencies and 27 voltages are applied, most of which can be changed through the software interface of the APi-TOF. In this study, the voltages applied were changed/optimized to obtain minimum possible fragmentation of the charged clusters while maintaining a good transmission of clusters across the instrument. The voltage setting values were chosen based on the results presented in the paper (Passananti et al., 2019).

S4. Fragmentation pathways and fragmentation rate

Under our experimental conditions most of the charged clusters produced by ESI were fragmented inside the APi-TOF. The bigger the charged cluster is, the larger the number of feasible fragmentation pathways. It is important to note that not all fragmentation pathways are important, as the process depends on many factors, such as the stability of the cluster and its fragments. To determine the significant pathways for the charged clusters, we used both an experimental and a modelling approach. A 2D plot of experimental results gave us an overview of the fragments that are detected at each voltage (i.e. mobility). We then proceeded to do fixed voltage scan experiments using the DMA P5 (SEADM) to determine and identify all charged clusters. On the other hand, the model enabled us to compute the kinetic rate constants for all the theoretical pathways. Figure S1 shows all the fragmentation rates (per second) against the internal energy (in Kelvin), in addition to the probability distribution of the internal energy of the clusters. The plot allowed us to compare all pathways and select the ones that are possible under our conditions (given the time available for fragmentation and the average energy of the cluster). We consider a fragmentation pathway possible when the significant fragmentation rate overlaps with the probability distribution of the internal energy of the clusters. We set the threshold for the fragmentation rate at 10^3 s^{-1} (which is about three orders of magnitude lower than the typical collision rate) and therefore we assume that clusters will not fragment before the next collision (the probability of fragmentation is ~ 0.1%). Table S1 lists all the fragmentation pathways that are observed in our experiment for each detected charged cluster. In the table below and throughout the whole paper we refer to sulfuric acid as S, dimethylamine as D, bisulfate ion as B and clusters as for example 2D2S1B, which corresponds to a cluster of two dimethylamine molecules, two sulfuric acid molecules and one bisulfate ion.

Table S1. Fragmentation pathways for all sulfuric acid and dimethylamine clusters.

Cluster	Fragmentation Pathways
1S1B	→ 1S + 1B
2S1B	→ 1S + 1S1B
	→ 2S + 1B
1D2S1B	→ 1D + 2S1B
	→ 1D1S + 1S1B
	→ 1D2S + 1B
1D3S1B	→ 1S + 1D2S1B
	→ 1D + 3S1B
	→ 1D1S + 2S1B
	→ 1D2S + 1S1B
2D1S1B	→ 2D + 1S1B
	→ 2D1S + 1B
2D2S1B	→ 1D + 1D2S1B
	→ 1D1S + 1D1S1B
	→ 2D1S + 1S1B
	→ 2D + 2S1B
	→ 2D2S + 1B
2D3S1B	→ 1D + 1D3S1B
	→ 1S + 2D2S1B
	→ 1D1S + 1D2S1B
	→ 1D2S + 1D1S1B
	→ 2D2S + 1S1B
	→ 2D1S + 2S1B
	→ 2D3S + 1B
3D3S1B	→ 1D + 2D3S1B
	→ 1D1S + 2D2S1B
	→ 2D1S + 1D2S1B
	→ 3D2S + 1S1B
	→ 3D3S + 1B
4D4S1B	→1D + 3D4S1B

	→ 4D3S + 1S1B → 3D2S + 1D2S1B → 4D4S + 1B

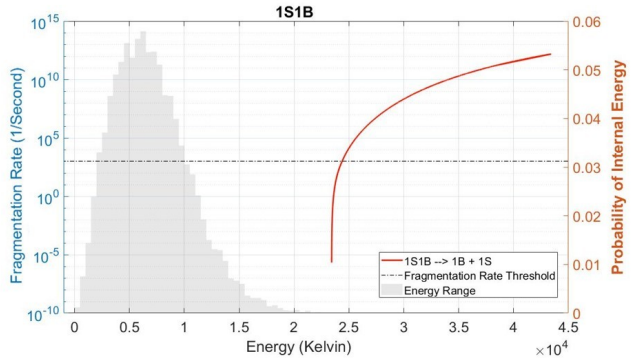
1S1B
Fragmentation Rate (1/Second)
Probability of Internal Energy
Energy (Kelvin)
×10^4
1S1B --> 1B + 1S
Fragmentation Rate Threshold
Energy Range

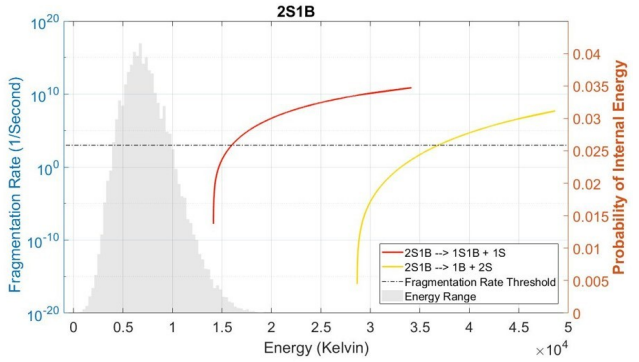
2S1B
Fragmentation Rate (1/Second)
Probability of Internal Energy
Energy (Kelvin)
×10^4
2S1B --> 1S1B + 1S
2S1B --> 1B + 2S
Fragmentation Rate Threshold
Energy Range

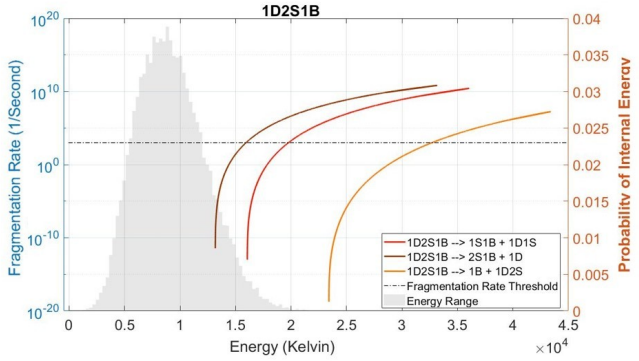
1D2S1B
Fragmentation Rate (1/Second)
Probability of Internal Energy
Energy (Kelvin)
×10^4
1D2S1B --> 1S1B + 1D1S
1D2S1B --> 2S1B + 1D
1D2S1B --> 1B + 1D2S
Fragmentation Rate Threshold
Energy Range

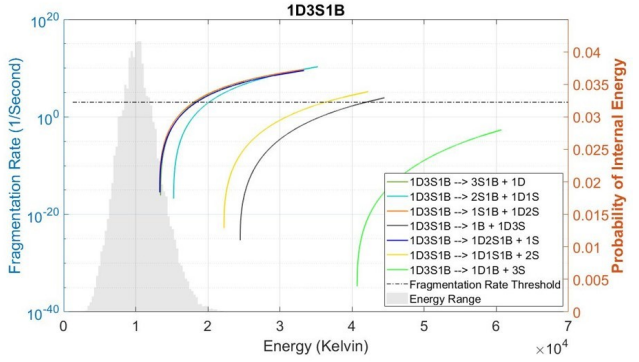
1D3S1B
Fragmentation Rate (1/Second)
Probability of Internal Energy
Energy (Kelvin)
×10^4
1D3S1B --> 3S1B + 1D
1D3S1B --> 2S1B + 1D1S
1D3S1B --> 1S1B + 1D2S
1D3S1B --> 1B + 1D3S
1D3S1B --> 1D2S1B + 1S
1D3S1B --> 1D1S1B + 2S
1D3S1B --> 1D1B + 3S
Fragmentation Rate Threshold
Energy Range

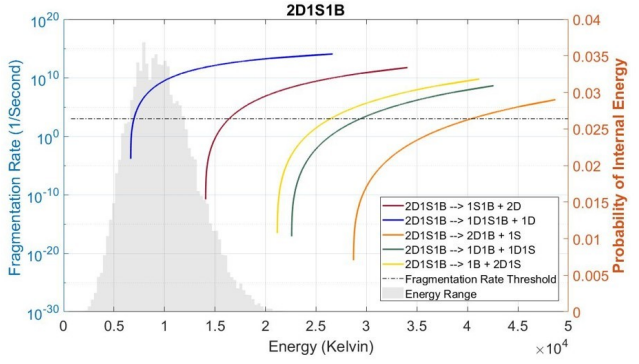
2D1S1B
Fragmentation Rate (1/Second)
Probability of Internal Energy
Energy (Kelvin)
×10^4
2D1S1B --> 1S1B + 2D
2D1S1B --> 1D1S1B + 1D
2D1S1B --> 2D1B + 1S
2D1S1B --> 1D1B + 1D1S
2D1S1B --> 1B + 2D1S
Fragmentation Rate Threshold
Energy Range

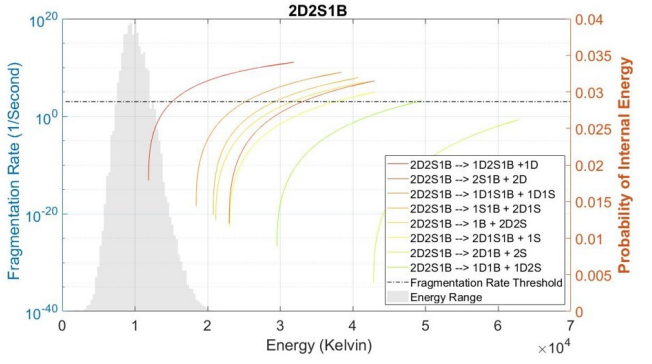
2D2S1B
Fragmentation Rate (1/Second)
Probability of Internal Energy
Energy (Kelvin)
×10^4
2D2S1B --> 1D2S1B +1D
2D2S1B --> 2S1B + 2D
2D2S1B --> 1D1S1B + 1D1S
2D2S1B --> 1S1B + 2D1S
2D2S1B --> 1B + 2D2S
2D2S1B --> 2D1S1B + 1S
2D2S1B --> 2D1B + 2S
2D2S1B --> 1D1B + 1D2S
Fragmentation Rate Threshold
Energy Range

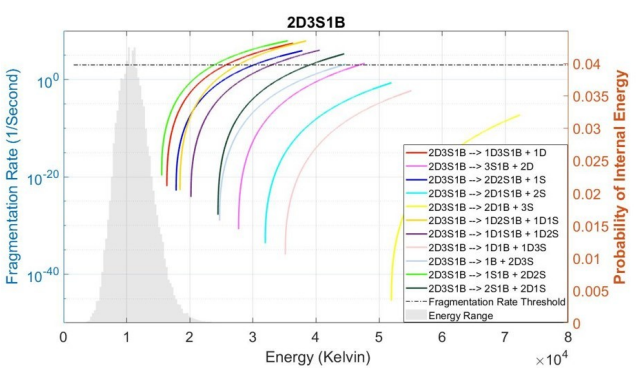
2D3S1B
Fragmentation Rate (1/Second)
Probability of Internal Energy
Energy (Kelvin)
×10^4
2D3S1B --> 1D3S1B + 1D
2D3S1B --> 3S1B + 2D
2D3S1B --> 2D2S1B + 1S
2D3S1B --> 2D1S1B + 2S
2D3S1B --> 2D1B + 3S
2D3S1B --> 1D2S1B + 1D1S
2D3S1B --> 1D1S1B + 1D2S
2D3S1B --> 1D1B + 1D3S
2D3S1B --> 1B + 2D3S
2D3S1B --> 1S1B + 2D2S
2D3S1B --> 2S1B + 2D1S
Fragmentation Rate Threshold
Energy Range

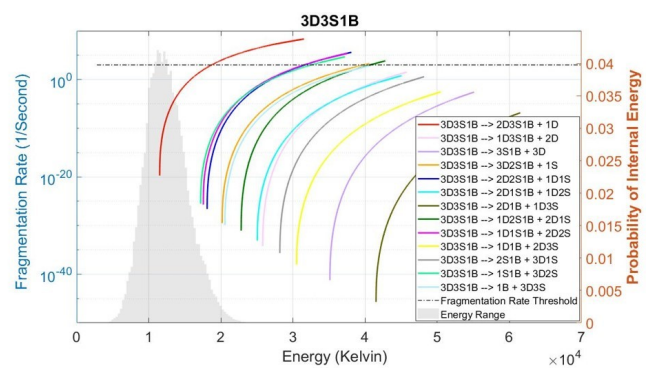
3D3S1B
Fragmentation Rate (1/Second)
Probability of Internal Energy
Energy (Kelvin)
×10^4
3D3S1B --> 2D3S1B + 1D
3D3S1B --> 1D3S1B + 2D
3D3S1B --> 3S1B + 3D
3D3S1B --> 3D2S1B + 1S
3D3S1B --> 2D2S1B + 1D1S
3D3S1B --> 2D1S1B + 1D2S
3D3S1B --> 2D1B + 1D3S
3D3S1B --> 1D2S1B + 2D1S
3D3S1B --> 1D1S1B + 2D2S
3D3S1B --> 1D1B + 2D3S
3D3S1B --> 2S1B + 3D1S
3D3S1B --> 1S1B + 3D2S
3D3S1B --> 1B + 3D3S
Fragmentation Rate Threshold
Energy Range

Figure S1. Fragmentation rate (s^{-1}, coloured lines) and probability distribution of internal energy (grey histogram) versus internal energy (Kelvin) for all detected clusters and their possible fragmentation pathways. The black dashed line shows the threshold rate we used in our calculations.

S5. Mass defect plot reconstruction

As mentioned in the main text, the first step was to correct all the measured mass spectrum intensities of the detected clusters for the transmission of the instrument. We then proceeded to use the survival probabilities of the clusters that we have calculated from the fixed voltage scan experiments to reconstruct the mass spectrum intensities of each cluster (Table S2). Finally, we converted the mass spectrum intensities to those of the mass defect intensities using a logarithmic relation (Table S3).

Table S2: Transmission corrected and reconstructed mass spectrum intensities for all detected clusters

Cluster	***m/z* (Th)**	**DMA Voltage (V)**	**Transmission corrected mass spectrum intensity (Original)**	**Mass spectrum intensity (Reconstructed)**	**Variation**
1B	96.96	-2075	22117.68	21690.45	–427.23
1S1B	194.93	-2310	9827.22	10054.60	227.38
2S1B	292.89	-2720	83.59	43.43	–40.15
1D2S1B	337.95	-3160	229.23	283.93	54.70
1D3S1B	435.92	-3585	4.44	3.60	–0.84
2D1S1B	285.04	-3265	8.24	22.49	14.25
2D2S1B	383.01	-3450	83.41	263.73	180.33
2D3S1B	480.98	-3740	15.56	29.57	14.01
3D3S1B	526.04	-3945	25.48	36.61	11.13
3D4S1B	624.00	-4505	2.45	0.00	–2.45
4D4S1B	669.06	-4505	4.16	6.16	2.00

Table S3: Original and reconstructed mass defect intensities for all detected clusters

Cluster	*m/z* (Th)	Mass Defect	Mass defect intensity (Original)	Mass defect intensity (Reconstructed)	Variation
1B	96.96	–0.04	26.73	26.69	–0.04
1S1B	194.93	–0.07	25.30	25.34	0.05
2S1B	292.89	–0.11	15.71	14.39	–1.32
1D2S1B	337.95	–0.05	17.76	18.19	0.43
1D3S1B	435.92	–0.08	9.67	9.25	–0.42
2D1S1B	285.04	0.04	11.01	13.05	2.04
2D2S1B	383.01	0.01	15.68	18.02	2.34
2D3S1B	480.98	–0.02	12.13	13.44	1.30
3D3S1B	526.04	0.04	13.02	13.75	0.74
3D4S1B	624.00	0.00	7.88	0.00	–7.88
4D4S1B	669.06	0.06	8.69	9.49	0.80

S6. APi-TOF MS transmission

When a certain number of charged ions or clusters enter an APi-TOF MS, some of those ions fail to reach the end detector. This loss of charged ions can be affected by the voltage configurations of the instrument and can be mass dependent. In other words, for a certain voltage configuration, smaller ions (lower mass/charge) may have higher transmission compared to larger ions (larger mass/charge) and for other voltage configurations an opposite trend (higher transmission for larger ions compared to smaller ones) could be observed (Passananti et al., 2019).

Mass discrimination effects arise through different parts of an APi-TOF MS. It is most evident in the two quadrupole regions of the APi interface as well as the orthogonal extraction unit in the TOF and multi-channel plate (MCP) detector (Heinritzi et al., 2016). The transmission (T) of an APi-TOF MS can thus be defined as the ratio between the detected ions and the ions entering the inlet, taking into account all losses of ions (Passananti et al., 2019).

For measuring the transmission of our instrument, a set-up that consists of a nickel–chromium wire generator connected to a Herrmann-DMA (Kangasluoma et al., 2016), an electrometer and finally an APi-TOF MS was used. The signals of the charged clusters produced by this system were detected and registered by both the electrometer and the APi-TOF. Those signals were then used to measure the transmission by comparing the difference in signal intensities of the charged clusters entering the instrument at the inlet (measured by the electrometer) to those detected at the end of the APi-TOF by the MCP.

After analysing the results a transmission efficiency plot was created (see Fig. S2 below) which was then used for the correction of the signal intensities of all detected clusters in our experiment.

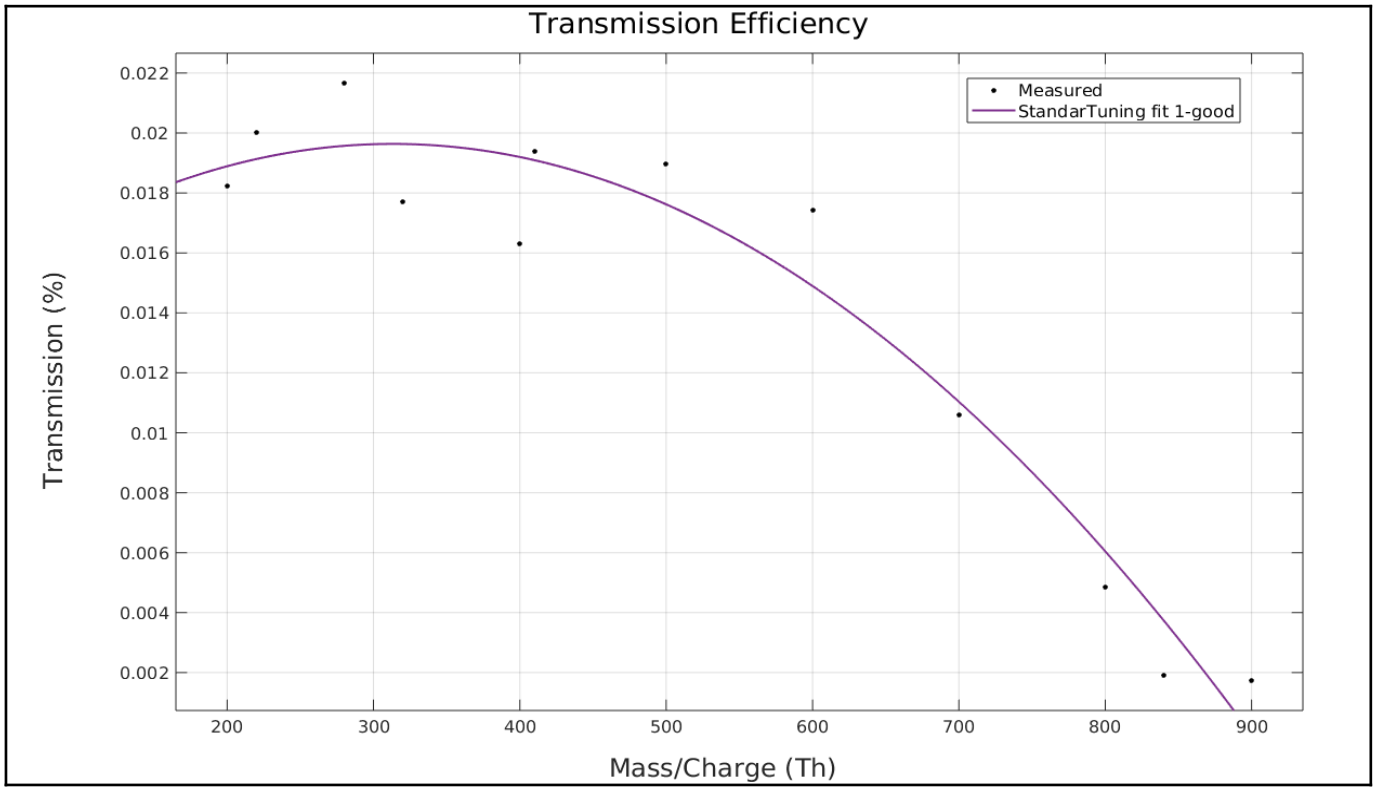

Figure S2. Transmission (%) of the APi-TOF MS versus mass/charge [Th] done using a wire generator connected to a Herrmann DMA, an electrometer and an APi-TOF MS.

S7. Model and quantum chemical calculations

As mentioned in the main text, our statistical model needs input data about the conditions of the experiment (i.e. carrier gas, pressure in the chambers, voltage settings), and information about the clusters' density of states. Quantum chemical calculations are needed to provide the rotational and vibrational energy states of the clusters.

We used quantum chemistry data taken from (Myllys et al., 2019). These data are the global free-energy-minimum structures of our studied clusters, with the geometry optimization and vibrational frequency analysis were carried out at the ωB97X-D/6-31++G(d,p) level of theory. Additionally, to obtain accurate binding energies, the electronic energies were corrected at the DLPNO–CCSD(T) method with the aug-cc-pVTZ basis set (more details on the technical aspects of the quantum chemistry calculations can be found in (Myllys et al., 2019).

References

Amo-González, M. and Pérez, S.: Planar Differential Mobility Analyzer with a Resolving Power of 110, Anal. Chem., 90, 6735–6741, https://doi.org/10.1021/acs.analchem.8b00579, 2018.

Heinritzi, M., Simon, M., Steiner, G., Wagner, A. C., Kürten, A., Hansel, A., and Curtius, J.: Characterization of the mass-dependent transmission efficiency of a CIMS, Atmos. Meas. Tech., 9, 1449–1460, https://doi.org/10.5194/amt-9-1449-2016, 2016.

Junninen, H., Ehn, M., Petäjä, T., Luosujärvi, L., Kotiaho, T., Kostiainen, R., Rohner, U., Gonin, M., Fuhrer, K., Kulmala, M., and Worsnop, D. R.: A high-resolution mass spectrometer to measure atmospheric ion composition, Atmos. Meas. Tech., 3, 1039–1053, https://doi.org/10.5194/amt-3-1039-2010, 2010.

Kangasluoma, J., Attoui, M., Korhonen, F., Ahonen, L., Siivola, E., and Petäjä, T.: Characterization of a Herrmann-type high-resolution differential mobility analyzer, Aerosol Science and Technology, 50, 222–229, https://doi.org/10.1080/02786826.2016.1142065, 2016.

Myllys, N., Kubečka, J., Besel, V., Alfaouri, D., Olenius, T., Smith, J. N., and Passananti, M.: Role of base strength, cluster structure and charge in sulfuric-acid-driven particle formation, Atmos. Chem. Phys., 19, 9753–9768, https://doi.org/10.5194/acp-19-9753-2019, 2019.

Passananti, M., Zapadinsky, E., Zanca, T., Kangasluoma, J., Myllys, N., Rissanen, M. P., Kurtén, T., Ehn, M., Attoui, M., and Vehkamäki, H.: How well can we predict cluster fragmentation inside a mass spectrometer?, Chem. Commun., 55, 5946–5949, https://doi.org/10.1039/C9CC02896J, 2019.